



## Article

# Impact of Physico-Chemical Properties of Cellulose Nanocrystal/Silver Nanoparticle Hybrid Suspensions on Their Biocidal and Toxicological Effects

Dafne Musino<sup>1</sup>, Julie Devcic<sup>2</sup>, Cécile Lelong<sup>2</sup>, Sylvie Luche<sup>2</sup>, Camille Rivard<sup>3,4</sup>, Bastien Dalzon<sup>2</sup>, Gautier Landrot<sup>3</sup>, Thierry Rabilloud<sup>2,\*</sup> and Isabelle Capron<sup>1,\*</sup>

- <sup>1</sup> INRAE, Institut National de Recherche Pour L'agriculture, L'alimentation et L'environnement, BIA, Biopolymères Interactions et Assemblages, 44316 Nantes, France; dafne.musino@inrae.fr
- <sup>2</sup> Laboratoire de Chimie et Biologie des Métaux, University Grenoble Alpes, CNRS, CEA, IRIG, CBM, UMR5249, 38000 Grenoble, France; devcicjulie@gmail.com (J.D.); cecile.lelong@univ-grenoble-alpes.fr (C.L.); sylvie.luche@cea.fr (S.L.); bastien.dalzon@cea.fr (B.D.)
- <sup>3</sup> SOLEIL Synchrotron, L'Orme des Merisiers, Gif-sur-Yvette, 91192 Saint-Aubin, France; Camille.Rivard@Synchrotron-Soleil.Fr (C.R.); gautier.landrot@synchrotron-soleil.fr (G.L.)
- <sup>4</sup> INRAE, Institut National de Recherche Pour L'agriculture, L'alimentation et L'environnement, BIA, TRANSFORM, 44316 Nantes, France
- \* Correspondence: thierry.rabilloud@cnrs.fr (T.R.); isabelle.capron@inrae.fr (I.C.)



**Citation:** Musino, D.; Devcic, J.; Lelong, C.; Luche, S.; Rivard, C.; Dalzon, B.; Landrot, G.; Rabilloud, T.; Capron, I. Impact of Physico-Chemical Properties of Cellulose Nanocrystal/Silver Nanoparticle Hybrid Suspensions on Their Biocidal and Toxicological Effects. *Nanomaterials* **2021**, *11*, 1862. <https://doi.org/10.3390/nano11071862>

Academic Editor: Alexey Pestryakov

Received: 16 June 2021

Accepted: 16 July 2021

Published: 20 July 2021

**Publisher's Note:** MDPI stays neutral with regard to jurisdictional claims in published maps and institutional affiliations.



**Copyright:** © 2021 by the authors. Licensee MDPI, Basel, Switzerland. This article is an open access article distributed under the terms and conditions of the Creative Commons Attribution (CC BY) license (<https://creativecommons.org/licenses/by/4.0/>).

**Abstract:** There is a demand for nanoparticles that are environmentally acceptable, but simultaneously efficient and low cost. We prepared silver nanoparticles (AgNPs) grafted on a native bio-based substrate (cellulose nanocrystals, CNCs) with high biocidal activity and no toxicological impact. AgNPs of 10 nm are nucleated on CNCs in aqueous suspension with content from 0.4 to 24.7 wt%. XANES experiments show that varying the NaBH<sub>4</sub>/AgNO<sub>3</sub> molar ratio affects the AgNP oxidation state, while maintaining an fcc structure. AgNPs transition from 10 nm spherical NPs to 300 nm triangular-shaped AgNP prisms induced by H<sub>2</sub>O<sub>2</sub> post-treatment. The 48 h biocidal activity of the hybrid tested on *B. Subtilis* is intensified with the increase of AgNP content irrespective of the Ag<sup>+</sup>/Ag<sub>0</sub> ratio in AgNPs, while the AgNSphere–AgNPPrism transition induces a significant reduction of biocidal activity. A very low minimum inhibitory concentration of 0.016 mg AgNP/mL is determined. A new long-term biocidal activity test (up to 168 h) proved efficiency favorable to the smaller AgNPs. Finally, it is shown that AgNPs have no impact on the phagocytic capacity of mammalian cells.

**Keywords:** CNC/AgNP hybrids; NaBH<sub>4</sub>/AgNO<sub>3</sub> molar ratio; H<sub>2</sub>O<sub>2</sub> redox; oxidation state; short- and long-term biocidal effect; MIC; toxicology

## 1. Introduction

In the last decades, silver nanoparticles (AgNPs) have emerged as one of the most efficient biocidal agents, limiting or preventing microorganisms' growth [1–4]. AgNPs are widely used in several applications (e.g., paints [5], cosmetics [6], dental material [7], water treatment [8]) because of their high surface-to-volume ratio [9,10] and their relatively low toxicity for human health [11]. Even if the exact action mechanism of AgNPs on bacteria is still not completely understood, several authors consider that their antimicrobial effect is mainly due to the release of the Ag<sup>+</sup> ions. These ions can interact with the components of the cell (e.g., thiols) [12], inducing structural and morphological changes in bacteria [10,12,13] and leading to its subsequent inactivation [13] (i.e., bacterial cell lysis).

Depending on the application (e.g., surgical sutures) [14], a long-term constant antimicrobial activity could be required and, consequently, AgNPs are added in large excess in the system. This approach could lead to an excessive instantaneous Ag<sup>+</sup> release or to a persistence of unused AgNPs, which can have a negative impact on human health [15,16] and on the environment [17,18]. An efficient alternative to obtain the biocidal properties ensured

by AgNPs and by most of the metallic NPs has not yet been found. Thus, the minimization of the amount of AgNPs without being detrimental to their bactericidal effect remains a challenge at this time. In this context, a good alternative may be provided by biocidal hybrid nanomaterials, where AgNPs are grafted onto the surface of a bio-based substrate, maximizing the AgNP specific surface and ensuring their good dispersion and stabilization, even without the addition of capping agents. Furthermore, the expected degradation of the bio-based substrate at the end-of-life of the material may provide the synthesis of more eco-friendly biocides. The use of polysaccharides as reducing and stabilizing agents for AgNPs, such as cellulose nanocrystals (CNCs), is a promising way [19–21]. CNCs are available, sustainable, and biodegradable, with high specific surfaces, low density, and low cost. They can be extracted from several renewable natural sources [22], they are well-dispersible in water with the ability to self-assemble [23], and they thus represent an excellent bio-based support to be used in hybrid nanomaterials.

Several methods have been developed to obtain the formation of AgNPs anchored on CNC surfaces, forming a hybrid nanoparticle (CNC/AgNP). As for the synthesis of isolated AgNPs, chemical reduction (e.g., by sodium borohydride [24], hydrazine [25], or dimethylformamide [26]) is one of the most efficient methods to nucleate AgNPs on CNC surface. Generally, an Ag precursor (silver nitrate,  $\text{AgNO}_3$ ) is added to the CNC suspension and the chemical reduction of the  $\text{Ag}^+$  ions is performed by sodium borohydride ( $\text{NaBH}_4$ ) [27–29],  $\text{NH}_4\text{OH}$  [30], polydopamine [31], or hydrazine [32]. Otherwise, CNCs are themselves indicated as both supports and reducers for the generation of metallic nanoparticles [33]. In most of the studies reported in the literature, CNCs are preliminary surface-modified (e.g., periodate oxidation, polydopamine coating) to ensure the grafting of AgNPs even if it has been experimentally proven that the AgNP nucleation on CNC surface occurs thank to the CNC surface hydroxyl groups and no surface treatment is necessary [34].

The characteristics of AgNPs (e.g., size, shape, structure) are crucial for their resulting antimicrobial activity and they strongly depend on the synthesis methods. Several works [35–37] reported that the smallest AgNPs provide the best efficiency in  $\text{Ag}^+$  release as given by the lowest inhibitory concentration (MIC) to ensure a detectable biocidal activity against various bacteria strains (e.g., *Streptococcus mutants*, *Escherichia coli*, *Staphylococcus aureus*), regardless of the fact that AgNPs are stabilized on CNCs [31,38,39] or by other capping agents or stabilizers. In line with the generic biocidal activity of  $\text{Ag}^+$  ions, AgNPs are toxic not only for bacteria, but also for eukaryotic cells. Comparing AgNP with different sizes (i.e., 10, 50, 100 nm), Kim et al. [40] proved that the strongest toxicological effect against eukaryotic cells was provided by the smallest NPs as the kinetics of AgNP dissolution and the consequent  $\text{Ag}^+$  release mechanism are driven by the NP surface-to-volume ratio.

The CNCs can also raise toxicological concerns. Their toxicity profile, including pulmonary, oral, dermal, and cytotoxicity, has been described [41,42], indicating that pulmonary toxicity is the main pathway to be considered [43]. Indeed, CNCs have been shown to induce pulmonary inflammation, but of a much lower amplitude than the one caused by true pulmonary toxicants such as asbestos [44].

Along with size, AgNP shape and structural composition can also affect the resulting antimicrobial activity [45]. The morphological characteristics of AgNPs can be modified performing specific post-treatment on synthesized AgNPs. To this aim, several authors [24,28,46,47] propose a hydrogen peroxide ( $\text{H}_2\text{O}_2$ ) redox post-treatment as  $\text{H}_2\text{O}_2$  has oxidation/reduction capabilities thanks to the autocatalytic decomposition on the AgNP surface. Indeed, the addition of  $\text{H}_2\text{O}_2$  could induce a transition from spherical AgNPs to bigger Ag nanoprisms with a triangular shape (AgNPrisms) [47,48], which display a localized surface plasmon resonance peak (LSPR) in the UV spectrum. The literature concerning the biocidal activity of AgNPrisms is quite controversial. Some studies [45,49] comparing truncated triangular AgNPrisms, spherical AgNPs, and rod-shaped NPs conclude that AgNPrisms allow the most efficient inhibition of *E. coli* growth, attributing the strong

biocidal activity of AgNPPrisms to the relevant role of their sharp edges and vertices. In contrast, Raza et al. [50] show that AgNPPrisms with an average edge length of 150 nm display a less intense antibacterial activity than those associated with spherical AgNPs with an average diameter of 15–50 nm, highlighting the fact that small spherical AgNPs could also penetrate more easily into the bacteria. The AgNP surface charge [51], surface coating [52], and solubility [53] can influence the resulting bactericidal effect as well, as  $\text{Ag}^+$  release seems to be involved in the regulation of antibacterial activity [1,35,54]. A few other works [2,55] focus on the role of the AgNP oxidation state (i.e., ratio between metallic silver,  $\text{Ag}_0$ , and ionic silver,  $\text{Ag}^+$ , in AgNP), not clearly indicating the specific contribution of the  $\text{Ag}^+$  and  $\text{Ag}_0$  fractions in AgNPs to the final biocidal activity. Nevertheless, a deeper investigation of the dependence of biocidal activity on the basis of the characteristics of AgNPs is necessary.

In our work, we proposed a detailed study focused on the correlation between the physico-chemical and morphological characteristics of AgNPs well-nucleated on the surface of CNCs and the resulting biocidal and toxicological activity. We synthesized CNC/AgNP hybrids, controlling the size, the shape, and the amount of well-dispersed AgNPs without any preliminary modification and without the use of any additional stabilizer. For the first time, we investigate the initial  $\text{NaBH}_4/\text{AgNO}_3$  molar ratio as a tuning parameter of the oxidation state of AgNPs without affecting their size, shape, and structure. Differently,  $\text{H}_2\text{O}_2$  redox post-treatment allowed reaching the morphological and structural transition of primary 10 nm spherical AgNPs to 300 nm AgNPPrisms. The antibacterial properties of the synthesized CNC/AgNP hybrids tested on *B. subtilis* strain reveal a performant short-term activity (48 h) and allow the determination of a low MIC value. Moreover, we propose for the first time an experimental method to detect the long-term biocidal activity (up to 168 h). Finally, the toxicological activity of hybrid suspensions carried out on mammalian cells (macrophages) is described.

## 2. Materials and Methods

### 2.1. Chemicals

Cellulose nanocrystals (CNCs) were purchased from CelluForce (Montreal, QC, Canada, product no. 2015-009). These CNCs were obtained from bleached Kraft pulp by acid hydrolysis, neutralized to sodium form, and finally spray-dried (length =  $183 \pm 88$  nm; cross section =  $6 \pm 2$  nm; aspect ratio = 31) [23]. Silver nitrate ( $\text{AgNO}_3 \geq 99\%$ ), sodium borohydride ( $\text{NaBH}_4 \geq 96\%$ ), and hydrogen peroxide ( $\text{H}_2\text{O}_2$ ) were purchased from Sigma-Aldrich and used without further purification. All the aqueous suspensions and solutions were prepared using ultra-pure water.

### 2.2. Synthesis of CNC/AgNP Hybrid Suspensions and $\text{H}_2\text{O}_2$ Post-Reaction

To produce well-dispersed CNC/AgNP hybrid suspensions at various AgNP contents, an experimental procedure proposed in our previous study was used [56]. Briefly, a volume of 10 mL of CNC aqueous suspension (2 g/L) was dialyzed against water for 3 days and then mixed with various amounts of  $\text{AgNO}_3$  aqueous solution (50 mM, from 15 to 700  $\mu\text{L}$ ) and with 500  $\mu\text{L}$  of freshly-prepared  $\text{NaBH}_4$  aqueous solution (100 mM) to reduce  $\text{Ag}^+$  ions and to synthesize AgNPs. The  $\text{NaBH}_4$  aqueous solution was put in ice to minimize its decomposition. The synthesis was performed working at pH ~6. The resulting CNC/AgNP suspension was mixed for 24 h at room temperature and aluminum foil was used to protect the sample from oxidation due to room light.

The  $\text{H}_2\text{O}_2$  redox post-treatment was performed by adding 160  $\mu\text{L}$  of hydrogen peroxide to the primary CNC/AgNP suspension under stirring, immediately after the introduction of  $\text{NaBH}_4$ . The addition of  $\text{H}_2\text{O}_2$  initiated an exothermic reaction, leading to the formation of gas bubbles originating from the  $\text{H}_2\text{O}_2$  decomposition [24].

### 2.3. UV/Vis Spectroscopy

Light-visible absorbance spectra of hybrid suspensions were recorded in the 300–900 nm range using a Mettler-Toledo UV7 spectrophotometer equipped with a 10 mm quartz cell. All the samples were diluted (1:10) by ultra-pure water, which was also used as a blank reference.

### 2.4. Atomic Absorption Spectroscopy (AAS)

The AgNP content in each hybrid suspension was determined by AAS (ICE 3300 AAS, Thermo Fisher, Waltham, MA, USA). A volume of 1 mL of sample was digested by 40 mL of water/aqua regia mixture overnight (i.e., 30% vol. aqua regia; HCl/HNO<sub>3</sub>: 3/1) and then analyzed. A calibration curve was obtained using a silver standard solution (1000 µg/mL, Chem-Lab NV, Zedelgem, Belgium) at different concentrations, from 0.25 to 10 ppm. For each sample, two independent measurements were performed. As the final CNC/AgNP suspension was dialyzed after the synthesis, it can be assumed that the entire Ag amount detected by AAS came from the AgNP dissolved by H<sub>2</sub>O/aqua regia mixture. From here on, the Ag content will thus be indicated as AgNP content, which will be expressed in mg of AgNP per g or mL of hybrid suspension (wt%).

### 2.5. Scanning Transmission Electron Microscopy (STEM)

To perform STEM acquisitions, a volume of 10 µL of diluted hybrid suspension (0.5 g/L in CNC content) was deposited on glow-discharged carbon-coated grids (200 meshes, Delta Microscopies, Microscopies, Mauressac, France) for 2 min, and the excess was then removed by Whatman filter paper. The grids were dried overnight in air and a 0.5 nm platinum layer was then deposited by an ion-sputter coater (LEICA AM ACE600, Oberkochen, Germany). Images were recorded at 10 kV with a Quattro Scanning electron microscope (Thermo Fisher Scientific, Waltham, MA, USA) using a STEM detector. ImageJ software was used to analyze the STEM images. For each sample, several images were examined and the AgNP Feret's diameter (i.e., the greatest distance of two tangents to the contour of the measured particle) of approximately 100 AgNPs was evaluated to obtain an average value.

### 2.6. X-ray Absorption Near-Edge Structure (XANES) and Extended X-ray Absorption Fine Structure (EXAFS)

XANES measurements were performed in order to evaluate the oxidation state of AgNPs in CNC/AgNP hybrid suspension, while EXAFS made it possible to describe the AgNP bulk atomic structure considering bond length and interatomic distance. XANES and EXAFS spectra were simultaneously acquired in transmission mode at the Ag K-edge on the SAMBA beamline at the SOLEIL synchrotron (Saint Aubin, France). Energy calibration of the Si (220) monochromator was set to 25,516 eV at the first inflection point of the Ag foil XANES spectrum. To be analyzed, all the hybrid suspensions were freeze-dried and then pressed to obtain 6 mm circular pellets with an AgNP content that made it possible to reach an absorption edge jump close to 1. Subsequently, pellets were positioned on a sample rod and then placed in a liquid nitrogen bath before being introduced into the He cryostat (T = 20 K).

Two standards were considered, silver foil (Agfoil) and AgNO<sub>3</sub> aqueous solution with 1 wt% glycerol (AgH<sub>2</sub>O). One scan was collected for each sample in transmission and continuous scan mode in the energy range of 25,250 to 27,750 eV with 5 eV/s monochromator velocity and 0.08 s/point integration time. Scans were normalized and background-subtracted using Athena [57] software. A linear combination fitting (LCF) procedure was then performed to analyze XANES spectra, in the fit range of [E<sub>0</sub> – 20 eV, E<sub>0</sub> + 50 eV], with E<sub>0</sub> set to 25,514 eV and using Agfoil and AgH<sub>2</sub>O standards as components for fitting. All the component weights were forced to be positive and the relative proportions of the components were forced to add up to 100%.

EXAFS data were first background-subtracted using an autobk algorithm (Rbkb = 1, k-weight = 3), and the Fourier transform of the k<sup>3</sup>-weighted EXAFS spectra was then

calculated over a  $k$  range of 2.5–18  $\text{\AA}^{-1}$ , using a Hanning apodization window (width of the transition region window parameter = 1). The  $k^3$  EXAFS fitting was performed in the 2.35–7.7  $\text{\AA}$  distance range with the Artemis [57] interface to IFEFFIT using least-squares refinements. Paths used for fitting standards and samples were obtained from a metallic silver crystallographic model [58] using the FEFF6 algorithm included in the Artemis interface. The  $E_0$  value was fixed at 25,520 eV and only the paths with a rank higher than 7% were considered. In the fitting procedure, the amplitude reduction factor  $S_0^2$  was fixed to 0.978 after being determined by fitting the first coordination sphere of the Agfoil spectrum over a range of 2.30–2.83  $\text{\AA}$ . Degeneracy of the paths, energy shift  $\Delta E_0$ , R shift  $\Delta R$ , and thermal and static disorder  $\sigma^2$  were fitted for each of the selected paths for a total of 52 independent points and 19 variables. All R-factors were lower than 0.04.

### 2.7. X-ray Diffraction Spectroscopy (XRD)

A Bruker D8 Discover diffractometer was used to record XRD diffractograms of the CNC/AgNP dried samples (10 min of acquisition). Cu-K $\alpha$ 1 radiation (1.5405  $\text{\AA}$ ) was produced in a sealed tube at 40 kV and 40 mA, parallelized using a Göbel mirror parallel optic system and then collimated to produce a 500 mm beam diameter. The data were collected in a  $2\theta$  angle range from 3° to 70°. The AgNP crystallite size (CS) was determined using Scherrer's equation [59]:

$$CS = \frac{K\lambda}{\beta \cos \theta}$$

where  $K$  is the shape factor (0.9),  $\lambda$  is the X-ray wavelength (1.54  $\text{\AA}$ ),  $\beta$  is the full-width at half-maximum (FWHM), and  $\theta$  is the angle of the diffraction peak of the crystalline phase (Bragg's angle). The FWHM was determined considering the AgNP characteristic peak at  $2\theta = 38^\circ$ .

### 2.8. Ag<sup>+</sup> Release Analysis

Conductometric measurements were performed to determine Ag<sup>+</sup> release in pure water from AgNPs in hybrid suspensions. The conductivity of dialyzed CNC/AgNP hybrid suspensions was monitored at 22 °C at different times (i.e., 48, 96, 120, and 168 h) using a Metrohm 856 Conductivity Module and recorded by Tiamo<sup>TM</sup> Titration Software. The concentration of Ag<sup>+</sup> ions (mM) was deduced using a calibration curve obtained by the analysis of various amounts of a silver standard solution (1000  $\mu\text{g}/\text{mL}$ , Chem-Lab NV, Belgium) diluted in a 2 g/L CNC suspension (i.e., Ag<sup>+</sup> concentrations from 0 to 2.4 mM).

### 2.9. Biocidal Tests

For disk diffusion biocidal tests, the *Bacillus subtilis* strain was used (3610 strain, wild type, personal gift of Maria Laaberki). *B. subtilis* is a commonly used Gram-positive bacterial strain and it was selected because of its easy manipulation under L1 conditions, with minimal safety concerns. The cells were grown in LB medium: 10 g/L tryptone, 5 g/L yeast extract, and 5 g/L NaCl. A 3610 *Bacillus subtilis* culture grown overnight on liquid LB at 37 °C was diluted to  $A_{600\text{nm}} = 0.1$  in 10 mL of fresh LB medium and incubated at 37 °C and 200 rpm until the  $A_{600\text{nm}}$  reached the exponential phase ( $\approx 0.6$ ). A volume of 300  $\mu\text{L}$  of this culture (or  $10^8$  cells) was uniformly applied on the surface of an LB agar plate (22 mL LB-agar) before placing the 5 mm diameter paper disks (blotting paper, grade 703 from VWR). For each hybrid suspension, a controlled volume of 3  $\mu\text{L}$  was immediately deposited on the paper disks. All the tests were performed working at neutral pH. Ultra-pure water and 70% ethanol were used as negative and positive controls, respectively. After 48 h at 30 °C, the average diameter of the inhibition zone was measured using ImageJ software. It was confirmed that the pure CNC did not display any biocidal activity (data not shown).

For the biocidal activity persistence test, the biocide-impregnated paper disks from the above experiment were recovered, layered on a fresh bacteria plate exactly as described above, and rehydrated with 3  $\mu\text{L}$  of water. The plates were grown at 30 °C for 96, 120, or 168 h, and the average diameter of the inhibition zones was measured. It was estimated

that 168 h represented a good compromise between the requirements for investigating a long-term biocidal activity and the feasibility of the experiment associated with the necessity of paper disk rehydration.

All experiments were performed in triplicate (three independent growth cultures) with at least two technical replicates, and the size of the paper disk was subtracted from the inhibition halo values.

#### 2.10. Toxicological Tests

The effects of CNC/AgNP hybrids on mammalian cells were assessed using a murine macrophage cell line model. To do this, J774A1 cells were grown in Dulbecco modified Eagle medium (DMEM) supplemented with 10% (*v/v*) fetal calf serum. Cells were seeded at 500,000 cells/mL, allowed to grow for 24 h, and then treated with the hybrid suspensions for an additional 24 h before the readout. Cell viability was assessed in a flow cytometry mode using propidium iodide exclusion. Phagocytic ability was assessed by internalization of fluorescent latex beads (diameter: 1  $\mu\text{m}$ ) in flow cytometry mode. Interleukine-6 (IL-6) and tumor necrosis factor alpha (TNF) production were assessed using a commercial kit (CBA from Becton Dickinson, Le Pont de Clai, France). For each sample, three independent measurements were performed.

### 3. Results and Discussion

#### 3.1. Variation of AgNP Content in CNC/AgNP Hybrids

A range of CNC/AgNP hybrids was produced by adding various amounts of Ag precursor ( $\text{AgNO}_3$ ) to a CNC aqueous suspension, varying the AgNP content from 0.4 wt% to 24.7 wt%, as reported in Table 1. The reduction of  $\text{Ag}^+$  ions by  $\text{NaBH}_4$  led to an immediate color change of the suspension from translucent to yellow, indicating the formation of AgNPs. As shown in the inset of Figure 1a, the color suspension became darker with increasing AgNP content. The formation of AgNPs resulted from the aggregation of monomeric Ag particles obtained by a reduction to zero-valence Ag atoms [28], and was confirmed by the presence of a dominant in-plane absorption peak at  $\lambda_{\text{max}} \sim 400$  nm in the UV/vis spectra (Figure 1a) whose intensity increased with AgNP content. The STEM images of dried CNC/AgNP hybrids (Figure 1b) clearly showed well-dispersed AgNPs attached to the CNC surface. Such a result highlights the fact that CNC is an excellent substrate for AgNP nucleation, growth, and stabilization, without any CNC surface modification required [34]. Independently from the AgNP content, the average AgNP diameter measured from electron microscopic images was in the order of 10 nm (Figure S1a). It turned out that the increase of precursor concentration,  $\text{AgNO}_3$ , only determined the number of grafted AgNPs on CNC without affecting their size. After AgNP formation, characteristic Ag peaks were detectable in the XRD patterns for all the CNC/AgNP hybrid suspensions (Figure S1b). The peak at  $38.1^\circ$  usually associated with the (111) lattice plane of face-centered cubic (fcc) silver was recorded (JCPDS Card No. 89-3722). Other characteristic Ag peaks with weaker intensity were detected at  $44.1^\circ$  and  $64.2^\circ$ , corresponding to (200) and (220) crystalline planes, respectively, thus confirming the isotropic nature of the crystals [28]. The average crystal size (CS) was estimated to be equal to  $3.3 \pm 0.3$  nm.

It is known that AgNPs are composed of metallic  $\text{Ag}_0$ , but they could also contain a certain  $\text{Ag}^+$  ion content [2,55], thus influencing the final AgNP oxidation state. The oxidation state of AgNPs in the hybrid system was investigated here by the analysis of XANES spectra. As reported in Figure S1c, the XANES data referring to the hybrid sample were compared to the XANES spectra of pure silver references. The analysis of these data using the Athena software based on the LCF procedure allowed precisely quantifying the  $\text{Ag}^+$  and  $\text{Ag}_0$  fractions in AgNPs.

**Table 1.** Characteristics of cellulose nanocrystal (CNC)/AgNP hybrids at different AgNP contents.

AgNO <sub>3</sub> Vol. (μL, 50 mM)	NaBH <sub>4</sub> /AgNO <sub>3</sub> Molar Ratio	AgNP Content (mg Ag/g Hybrid, wt%) <sup>1</sup>	Avg. Feret's Diam. (nm) <sup>2</sup>	CS (nm) <sup>3</sup>	Ag <sub>0</sub> (%) <sup>4</sup>
15	67.7	0.4 ± 0.03	10.5 ± 4.8	3.5	-
30	33.4	0.9 ± 0.04	-	-	-
60	16.7	1.6 ± 0.02	-	-	-
110	9.1	3.0 ± 0.03	11.3 ± 8.3	-	91 ± 9
160	6.3	6.0 ± 0.01	10.0 ± 7.4	3.7	75 ± 8
240	4.2	8.7 ± 0.05	9.9 ± 7.3	3.1	65 ± 7
330	3.0	12.5 ± 0.16	12.1 ± 9.2	3.2	57 ± 6
550	1.8	18.6 ± 0.14	12.2 ± 8.2	-	32 ± 3
700	1.5	24.7 ± 0.34	11.2 ± 9.1	3.0	34 ± 3

- Not measured, <sup>1</sup> by atomic absorption spectroscopy (AAS), <sup>2</sup> by scanning transmission electron microscopy (STEM) image analysis, <sup>3</sup> crystal size determined by X-ray diffraction (XRD), <sup>4</sup> by X-ray absorption near-edge structure (XANES); the standard error is established as 10% of the measured value.

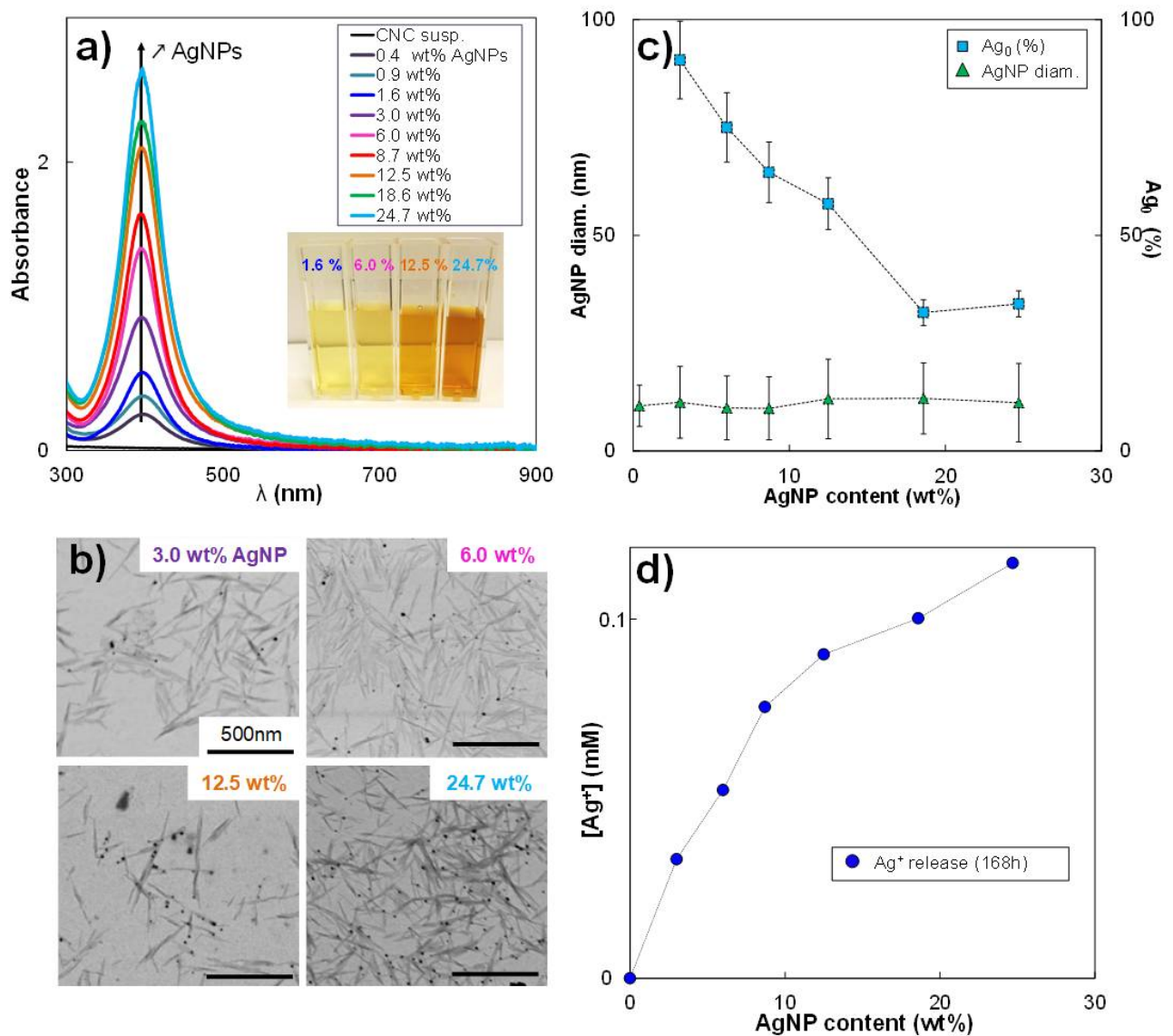


**Figure 1.** (a) UV/vis spectra and (b) STEM images of CNC/AgNP hybrids at various AgNP contents; (c) Evolution of AgNP average diameter and Ag<sub>0</sub> fraction in AgNPs as a function of the AgNP content in the hybrid suspension; (d) Ag<sup>+</sup> release plateau value at 168 h in pure water.

The resulting XANES spectra of all the samples are plotted in Figure S1d, the R-factor and the Chi-square values of the LCF fits are reported in Table S1, and the outcomes of the analysis are summarized in Table 1. It was not possible to process all the samples during the synchrotron session (limited beamtime); however, we assume that, for AgNP content below 3%, the fractions of Ag<sub>0</sub> were at least 90%. As shown in Figure 1c, the proportion of Ag<sub>0</sub> sharply decreased from around 90 to 30% with the increase of the initial AgNO<sub>3</sub> concentration (i.e., increase of the AgNP content) and the subsequent lowering of the NaBH<sub>4</sub>/AgNO<sub>3</sub> molar ratio. Even if the NaBH<sub>4</sub> reducing agent was always added in excess with respect to the AgNO<sub>3</sub>, allowing the formation of well-defined spherical nanoparticles (i.e., NaBH<sub>4</sub>/AgNO<sub>3</sub> molar ratio always higher than 1.5), the reduction process of the Ag<sup>+</sup> ions led to a variation of the AgNP oxidation state when the AgNP content was increased, suggesting that the nucleation and/or growth of AgNPs was strongly affected by the reducing conditions. It could be concluded that AgNPs were formed by both Ag<sub>0</sub> and Ag<sup>+</sup> fractions and that the final Ag<sub>0</sub>/Ag<sup>+</sup> ratio was influenced by the initial NaBH<sub>4</sub>/AgNO<sub>3</sub> molar ratio (Figure 1c). The presence of silver oxide, Ag<sub>2</sub>O, in AgNP was excluded using an Ag<sub>2</sub>O reference for the fitting of XANES spectra where the amount of silver oxide represented less than 1%.

The EXAFS Fourier transform spectra (Figure S2a–c) of the CNC/AgNP hybrid suspensions with increasing AgNP content were fitted with the crystallographic structure of metallic silver. For each CNC/AgNP sample, the fitted and experimental spectra were similar to each other (Figure S2). R-factors were all lower than 0.040 (Table S2), which reflected reasonable fits [60]. This indicated that the structure of each CNC/AgNP hybrid agreed with the structure of metallic silver. The shift in R space obtained from the fits for each atomic shell is systematically negligible. The results showed that the interatomic distances in the CNC/AgNP hybrids did not significantly change in comparison with the metallic silver distances and that the space group of the AgNPs still corresponded to the fcc silver structure, as indicated by XRD. Thus, the crystal structural organization was not affected by the AgNP content.

Finally, CNC/AgNP hybrids were plunged in water and their conductivity was measured over time to estimate the Ag<sup>+</sup> kinetic release from AgNPs. An increase in the Ag<sup>+</sup> concentration during the first 48 h was recorded (Figure S3), in agreement with the work of Zhang et al. [61]. After 120–168 h, all the samples reached an equilibrium state with a constant Ag<sup>+</sup> concentration, and the final concentration value increased with increasing AgNP content (Figure 1d). Such a result could be used to evaluate the amount of AgNP required for an Ag<sup>+</sup> release desired at equilibrium conditions.

### 3.2. Morphological Variation from Spherical AgNPs to AgNPPrisms by H<sub>2</sub>O<sub>2</sub> Redox Post-Treatment

As shown in STEM images (Figure 2), the H<sub>2</sub>O<sub>2</sub> redox action turned the primary ~10 nm AgNPs nucleated on CNC surfaces into bigger AgNPPrisms. Our group recently investigated variations of morphological and physico-chemical properties of AgNP as a function of the H<sub>2</sub>O<sub>2</sub>/AgNP mass ratio [56]. In the present work, we briefly summarized the main characteristics of the CNC/AgNP hybrid suspensions where an H<sub>2</sub>O<sub>2</sub> redox post-treatment was performed. These hybrids, referred to as CNC/AgNP\_H<sub>2</sub>O<sub>2</sub>, were obtained by mixing hybrids bearing 8.7, 12.5, 18.6, and 24.7 wt% AgNP with 160 µL of H<sub>2</sub>O<sub>2</sub>. The H<sub>2</sub>O<sub>2</sub>/AgNP mass ratio,  $\alpha$ , was equal to 0.27, 0.20, 0.12, and 0.09, respectively. After the H<sub>2</sub>O<sub>2</sub> treatment and dialysis of the suspension, the AgNP\_H<sub>2</sub>O<sub>2</sub> content was checked by AAS and found to be equal to 6.9, 9.3, 17.1, and 24.1 wt%, respectively. We can thus assume that roughly the same amount of AgNP is measured after the post-treatment.

The transition from ~10 nm spherical AgNPs (Figure 1b) to AgNPPrisms with an average diameter of 150–300 nm (Figure 2) was obtained only when the critical  $\alpha$  value of 0.20 was exceeded. Below this threshold value, the AgNPs\_H<sub>2</sub>O<sub>2</sub> maintained their spherical shape, with a size of approximately 15 nm. Moreover, the AgNP–AgNPPrism transition was associated with variations in the oxidation state. Indeed, the formation of AgNPPrisms corresponded to an increase in the Ag<sub>0</sub> content from 57–65% up to 100%, while



the Ag<sub>0</sub> fraction remained between 30 and 50% for the 15 nm spherical AgNPs\_H<sub>2</sub>O<sub>2</sub>. The characteristics of the hybrids with and without the H<sub>2</sub>O<sub>2</sub> redox post-treatment are reported in Table 2.

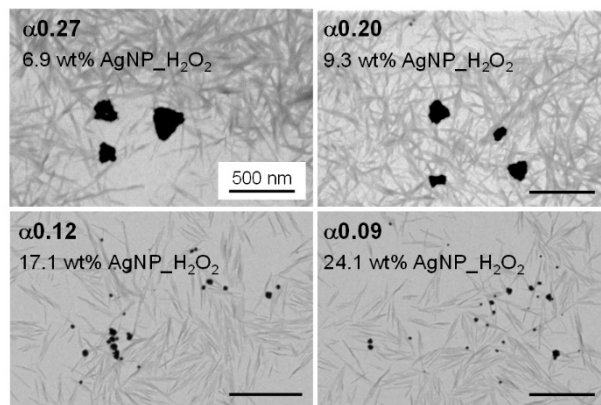


Figure 2. STEM images of CNC/AgNP hybrids at various  $\alpha$  values. The scale bar is 500 nm.

Table 2. Characteristics of hybrids with and without H<sub>2</sub>O<sub>2</sub> post-treatment.

AgNP Content (wt%)	H <sub>2</sub> O <sub>2</sub> Vol. ( $\mu$ L)	H <sub>2</sub> O <sub>2</sub> /AgNP Mass Ratio, $\alpha$	NP Shape/Size <sup>1</sup> (nm)	Ag <sub>0</sub> (%) <sup>2</sup>
8.7	0	0	Nanospheres (~10)	65 $\pm$ 7
12.5	0	0	Nanospheres (~10)	57 $\pm$ 6
18.6	0	0	Nanospheres (~10)	32 $\pm$ 3
24.7	0	0	Nanospheres (~10)	34 $\pm$ 3
6.9 (AgNP_H <sub>2</sub> O <sub>2</sub> )	160	0.27	Nanoprisms (~150–300)	95 $\pm$ 10
9.3 (AgNP_H <sub>2</sub> O <sub>2</sub> )	160	0.20	Nanoprisms (~150–300)	97 $\pm$ 10
17.1 (AgNP_H <sub>2</sub> O <sub>2</sub> )	160	0.12	Nanospheres (~15)	50 $\pm$ 10
24.1 (AgNP_H <sub>2</sub> O <sub>2</sub> )	160	0.09	Nanospheres (~15)	29 $\pm$ 3

<sup>1</sup> by STEM image analysis; <sup>2</sup> by XANES; the standard error is established as 10% of the measured value.

### 3.3. Short-Term Biocidal Activity: Impact of AgNP Content and Oxidation State

Biocidal tests were performed on *B. subtilis* for all hybrids bearing primary spherical AgNPs. *Bacillus subtilis* was chosen as a model organism for the following reasons: (i) it is easy and safe to handle (Biosafety level 1), (ii) it is a good model of Gram+ bacteria, and (iii) it has been demonstrated to be of similar sensitivity to metal-based nanobiocides to pathogenic microorganisms. This has been demonstrated both on copper [62] and silver [63] nanoparticles. The inhibition halo diameter measured at 48 h increased with the amount of AgNP (Figure 3a and Figure S4). According to the known bactericidal mechanism, the biocidal effect is directly linked to the released Ag<sup>+</sup> ions that interact with bacteria. Such a release mechanism might be simulated by the Ag<sup>+</sup> release when the hybrids are maintained in water, as previously mentioned. Figure 3a shows the Ag<sup>+</sup> ion concentration at 48 h in the aqueous medium that was monitored by conductimetry. The amount of Ag<sup>+</sup> released increased with the AgNP content in the hybrid, showing a slope change of around 10 wt% AgNP. This non-linear evolution of the Ag<sup>+</sup> ion release was also reflected in the non-linear enlargement of the inhibition halo. Thus, the Ag<sup>+</sup> release estimated by conductimetry was compared to the Ag<sup>+</sup> and Ag<sub>0</sub> fractions in AgNPs determined by XANES (Figure S5). The Ag<sup>+</sup> fraction in the AgNPs increased with the AgNP content, as observed for the [Ag<sup>+</sup>] released in water. However, conductometric measurements also showed that an Ag<sup>+</sup> release was detectable even when AgNPs were mainly composed of Ag<sub>0</sub> (at low AgNP contents), suggesting that both metallic and complexed ionic silver can provide the Ag<sup>+</sup> release and, consequently, an antimicrobial activity.

To better understand the impact of the AgNP oxidation state on the detected antimicrobial effect, we compared the biocidal activity at 48 h of hybrid suspensions containing

the same AgNP content, but composed of a different  $\text{Ag}^+$  fraction. It should be recalled that all AgNPs had a spherical shape with an average diameter of approximately 10 nm. Firstly, three hybrids with increasing AgNP content were selected: H1, H2, and H3 at 3, 8.7, and 18.6 wt% AgNP, respectively, where the fraction of  $\text{Ag}^+$  varied (Table 3). The sample containing the higher concentration in  $\text{Ag}^+$  (H3) was then diluted twice (H3/2) and six times (H3/6) to maintain the  $\text{Ag}^+$  fraction constant, but decreasing the AgNP contents to 8.7 and 3.0 wt% of AgNP, respectively (i.e., as in H1 and H2). For suspensions at the lowest AgNP content, H1 and H3/6, the width of the inhibition halos was 2.9 and 4.2 mm for 8.7 and 68%  $\text{Ag}^+$ , respectively (Table 3), which are in the error bars. Similarly, at a greater amount of AgNPs, the inhibition halos of H2 and H3/2 hybrids reached very close values of 7.1 mm and 7.4 mm for 35 and 68%  $\text{Ag}^+$ , respectively (Figure S6). Because of the slight variation of the inhibition halos of the samples within the error bar, a clear difference between the  $\text{Ag}_0$  and the  $\text{Ag}^+$  role in the biocidal activity could not be deduced, and the  $\text{Ag}_0/\text{Ag}^+$  ratio of AgNP did not seem to affect the resulting antimicrobial effect. As the AgNP oxidation state is governed by the amount of chemical reducer with respect to the metallic precursor (i.e., decrease in  $\text{Ag}_0$  content with the decrease of the  $\text{NaBH}_4/\text{AgNO}_3$  molar ratio), the very low amount of reducer can be used to obtain well-dispersed AgNP in hybrids and, as a result, CNC/AgNP hybrids with highly efficient biocidal properties.

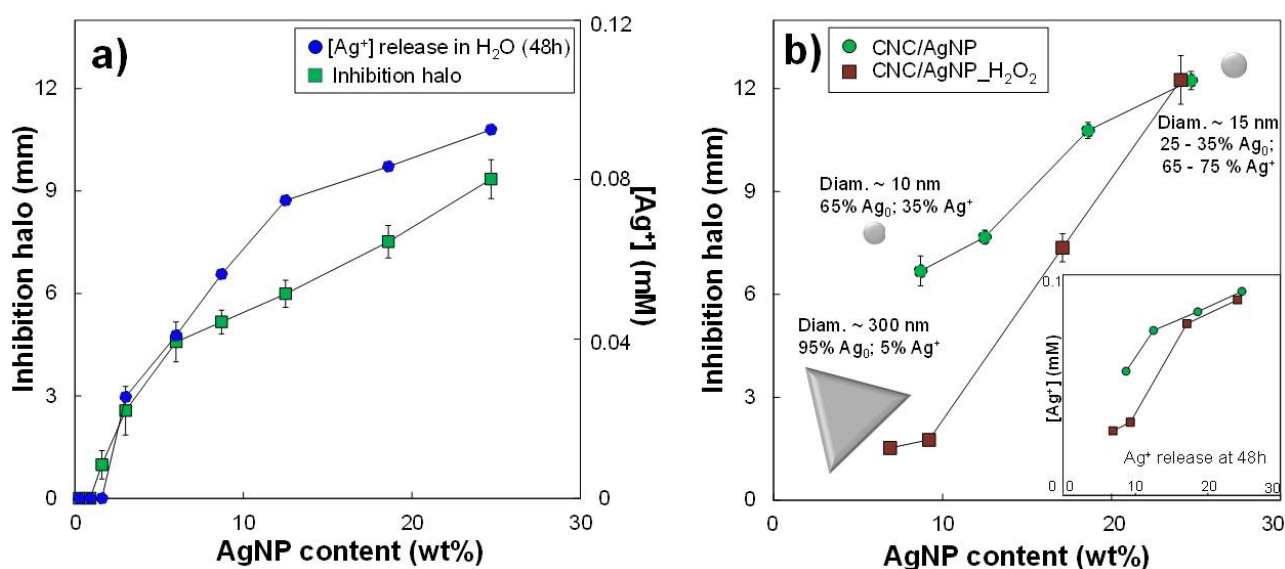


**Figure 3.** (a) Variation of the inhibition halo diameter and of the  $\text{Ag}^+$  ion concentration released in water measured by conductimetry as a function of the AgNP content in the CNC/AgNP hybrid suspensions. All AgNPs have an average diameter of ~10 nm. (b) Comparison between inhibition halos of CNC/AgNP at different AgNP contents with and without  $\text{H}_2\text{O}_2$  redox post-treatment. Inset: Evolution of  $\text{Ag}^+$  release in water at 48 h measured by conductimetry.

**Table 3.** Characteristics of hybrid samples used in biocidal tests to discriminate the antibacterial activity of  $\text{Ag}_0$  and  $\text{Ag}^+$  fractions in AgNPs.

Hybrid (Code)	AgNP Content (mg/g of Hybrid), %	$\text{Ag}^+$ (%) by XANES	Inhibition Halo (mm)
H1	3.0	9	$2.9 \pm 1.4$
H2	8.7	35	$7.1 \pm 0.2$
H3	18.6	68	$10.0 \pm 0.9$
H3/2 (eq. H2)	9.3	68	$7.4 \pm 0.8$
H3/6 (eq. H1)	3.1	68	$4.2 \pm 1.1$

The evaluation of the short-term biocidal activity allowed estimating the minimum inhibitory concentration (MIC). According to the results of the diffusion tests reported

in Figure 3a, the first inhibition halo was detected for the CNC/AgNP hybrid at 1.6 wt% AgNP (i.e., 0.016 mg AgNP/mL of hybrid). This MIC value is results one of the lowest values reported in literature for systems similar to the one presented in our work [31,38,64]. However, it is quite challenging to properly compare the MIC values as they strongly depend on the effective volume deposited on the diffusion disk during the biocidal activity test. Thus, the evaluation of the AgNP amount deposited on the diffusion disk can represent a more accurate parameter to determine the efficiency of the biocide. In our case, 3  $\mu$ L of hybrid suspension at 1.6 wt% AgNP was used to impregnate the paper disk for the test, thus only 0.048  $\mu$ g of AgNP was effectively deposited onto it. To the best of our knowledge, this is the lowest AgNP content that makes it possible to obtain a well-detectable biocidal effect compared with those proposed in other studies, as reported in Table S3, proving the antimicrobial efficiency our hybrid system linked to the good stabilization and dispersion of AgNPs on CNC surface.

#### 3.4. Short-Term Biocidal Activity: Impact of AgNP Size–Shape Variation by H<sub>2</sub>O<sub>2</sub>

A new independent test was performed to compare the antibacterial action at 48 h of CNC/AgNP hybrid suspensions with various amounts of AgNP (i.e., 8.7, 12.5, 18.6, and 24.7 wt%) with and without a fixed amount of H<sub>2</sub>O<sub>2</sub> for redox post-treatment (i.e.,  $\alpha$  equal to 0.27, 0.20, 0.12, and 0.09, respectively); Figure 3b. It should be recalled that this type of H<sub>2</sub>O<sub>2</sub> reaction induced the transition from spherical AgNPs with an average diameter of approximately 10 nm to 150–300 nm triangular Ag objects only for hybrids at  $\alpha$  values higher than 0.20. The characteristics of the investigated samples are reported in Table 2.

For the CNC/AgNP hybrid at the lowest amount of AgNP, 8.7 wt%, the size of the inhibition halo for the reference decreased from  $6.7 \pm 0.1$  mm to  $1.5 \pm 0.1$  mm once treated with H<sub>2</sub>O<sub>2</sub> (Figure 3b). It can be assumed that the variation of the biocidal activity could be mainly attributed to the AgNP size–shape transition to AgNP prisms, with an Ag<sub>0</sub> fraction in AgNPs of between 65% and 95%. This agreed with the general concept that, the smaller the NP, the stronger the biocidal effect results will be [2,13,36,37], because the Ag<sup>+</sup> release is a phenomenon occurring at the NP surface [61]. On the other hand, the AgNP size–shape transition did not occur when  $\alpha$  was equal to 0.12 and 0.09. Thus, the AgNPs\_H<sub>2</sub>O<sub>2</sub> maintained their morphological characteristics and the Ag<sub>0</sub> fraction of the primary AgNPs as before the H<sub>2</sub>O<sub>2</sub> treatment, thus providing an equivalent biocidal activity. Accordingly, conductometric measurements showed that the release of Ag<sup>+</sup> at 48 h for the larger AgNP prisms was significantly lower than that provided by spherical AgNP\_H<sub>2</sub>O<sub>2</sub> of about 10 nm (inset Figure 3b), which showed an Ag<sup>+</sup> release equivalent to that of primary AgNPs. These results suggested that the accessibility and, consequently, the specific surface of AgNPs is the main factor affecting AgNP biocidal activity, and not their internal structure at 48 h.

#### 3.5. Long-Term Biocidal Activity of CNC/AgNP Hybrids

A new protocol was designed to detect the biocidal activity over several days (see Material and Methods section). We focused on hybrids at 8.7 and 24.7 wt% AgNP with and without H<sub>2</sub>O<sub>2</sub> redox post-treatment (see Table 2). As indicated in the previous sections, all these hybrids displayed an antimicrobial activity at 48 h (Figure 3b). At 96 h, a decrease of biocidal activity of all the hybrids was detected after the transfer of the hybrid-impregnated disk to a fresh bacteria plate (Figure 4). In particular, no biocidal effect was detected for the hybrids containing AgNP prisms of 150–300 nm (6.9 wt% AgNP\_H<sub>2</sub>O<sub>2</sub>), suggesting that even the long-term activity was mainly governed by the AgNP size, even if it was still linked to the oxidative dissolution and, consequently, Ag<sup>+</sup> ion release. After 96 h, the Ag<sup>+</sup> release seemed to reach an equilibrium state for all the samples according to the conductimetry data (Figure S7). At this stage, the biocide-impregnated paper disk was rehydrated with 3  $\mu$ L of H<sub>2</sub>O and incubated again against bacteria. At 120 h and 168 h total incubation time, no biocidal effect was detected for the hybrid suspension characterized by AgNP prisms, while an antibacterial activity was still observed for the other samples

containing smaller spherical AgNPs. This experimental evidence once again underlined how the 10 nm nano-spherical shape ensured a more efficient short- and long-term biocidal effect compared with the 300 nm AgNPPrisms.

Furthermore, at 168 h, the hybrid suspension at a higher AgNP content with and without the H<sub>2</sub>O<sub>2</sub> redox post-treatment showed a more transparent inhibition zone around the disk compared with that displayed by the hybrid sample at lower AgNP content characterized by the presence of AgNPPrisms. (Figure S8). Such a difference could be explained by considering not only the inhibition of the bacterial growth around the disk, but also the elimination of all the residual bacterial colonies, showing a consistent biocidal effect (i.e., complete bacterial lysis or inhibition). Moreover, the inhibition halo of the CNC/AgNP\_H<sub>2</sub>O<sub>2</sub> was slightly wider than the one of the same sample without the H<sub>2</sub>O<sub>2</sub> post-treatment. This experimental evidence seemed to suggest that, even if a size–shape transition did not occur, the H<sub>2</sub>O<sub>2</sub> post-treatment favored the oxidative dissolution of AgNPs\_H<sub>2</sub>O<sub>2</sub>, and thus the Ag<sup>+</sup> release, thus leading to a clearer biocidal activity compared with the primary AgNPs at the same total silver content, especially in medium- (96 h) and long-term (120–168 h) experiments.

To summarize, the results of our biocidal diffusion tests clearly showed that the tuning of the morphological and physico-chemical properties of the AgNPs in the CNC/AgNP hybrids made it possible to control the resulting short- and/or long-term biocidal activity. In particular, it was demonstrated that the AgNP oxidation state did not affect the Ag<sup>+</sup> release associated with the antimicrobial activity, whereas the morphological transition from ~10 nm AgNPs to ~300 nm AgNPPrisms induced the inhibition of the biocidal properties of the hybrid system from 48 h up to 168 h, examining the critical role of the specific surface of AgNP. Moreover, it was shown that, when the H<sub>2</sub>O<sub>2</sub> post-treatment did not induce a morphological variation of AgNPs (i.e., no transition to AgNPPrisms), their biocidal properties were enhanced, making it possible to obtain a complete bacterial lysis around the diffusion disk. It shall be underlined that, in complex biological media such as those used for the biocidal activity tests, numerous organic and inorganic Ag ligands are present, which may limit the concentration of free Ag<sup>+</sup> ions at any time. The biological macromolecules bind silver with very high affinity owing to the cooperative nature of their interaction with silver ion [65], as demonstrated for example on polyamine acids [66]. Thus, even in a context where most of the liberated Ag<sup>+</sup> ions are complexed by the media components, bacterial macromolecules will still be able to displace the equilibrium toward their silver-loaded forms, and eventually inactivate them and lead to the biocidal activity.

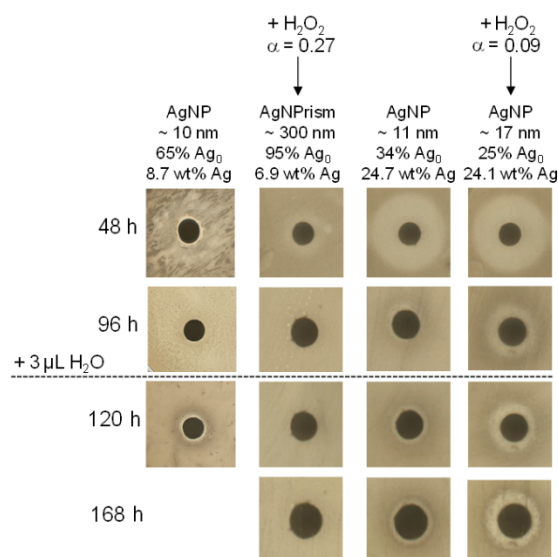


**Figure 4.** Evolution at various incubation times (48, 96, 120, 168 h) of inhibition halos of CNC/AgNP hybrids at two different initial AgNP contents (8.7 and 24.7 wt% Ag) with and without H<sub>2</sub>O<sub>2</sub> redox post-treatment.

### 3.6. Impact of the Variation of AgNP Content on Macrophage Viability and Function

By definition, a biocide is not specific for a given set of species. In that humans may come into contact with the biocide during its manufacture or use, it is interesting to examine its toxicity to mammalian cells. In this context, one of the most relevant cell types to test the toxicity of a particular biocide is represented by the macrophages, as these cells are in charge of removing foreign particulate material from the body. Firstly, we examined the toxicity of CNC/AgNP hybrids containing various amounts of AgNP (from 3 to 24.7 wt%) on macrophages, directly adding them to the macrophage culture medium in various concentrations. The concentrations of CNC/AgNP suspensions in the culture medium are reported in Table 4. The results of these experiments show a toxicity only for the higher AgNP contents, at 5% and 10% of the hybrids (Figure 5), i.e., for 50% cell death, as observed for the points at approximately 20  $\mu\text{g/mL}$  Ag concentration, as reported in Table 4). A moderate toxicity was observed at lower AgNP concentrations (20% cell death at approximately 10  $\mu\text{g/mL}$  Ag concentration, as reported in Table 4). Such a curvilinear response curve, with no toxicity observed at low doses and a relatively sudden onset of toxicity, has been observed on the same cell type with free AgNPs [67,68].

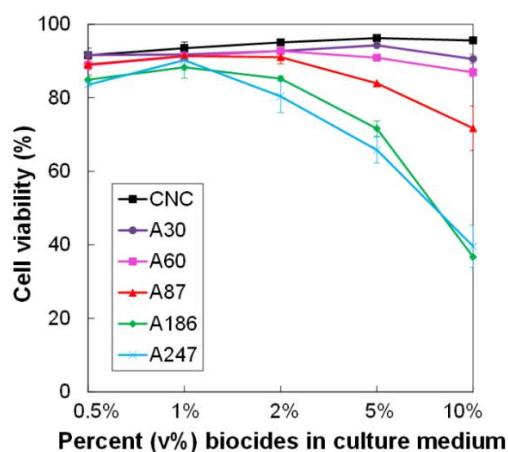


Figure 5. Assessment of toxicity of biocides on J774A1. Dose-dependent survival curve for cells treated for 24 h with various concentrations of hybrids.

Table 4. Concentrations of AgNP for various hybrid volume fractions analyzed for toxicity on J774A1.

Sample Code	Relative AgNP Content in Hybrid (wt%)	AgNP in Culture Medium ( $\mu\text{g/mL}$ )				
		0.5 v%	1 v%	2 v%	5 v%	10 v%
A30	3	0.2	0.3	0.6	1.5	3
A60	6	0.3	0.6	1.2	3	6
A87	8.7	0.4	0.9	1.7	4.4	8.7
A186	18.6	0.9	1.9	3.7	9.3	18.6
A247	24.7	1.2	2.5	4.9	12.4	24.7

Pure CNCs were used as a control and did not show toxicity, even at high concentrations (200  $\mu\text{g/mL}$ ). As shown by the comparison of the different biocides, the cytotoxic effect was relatively independent of the density of grafting, and depended instead on the AgNP concentration. The toxicity shown by the CNC/AgNP hybrids was in line with the results published in the literature [43]. Large AgNPs (diameter: 60 nm; PVP-coated) were less toxic for the same cells than the hybrids, with only 20% cell death at 20  $\mu\text{g/mL}$  Ag, [67] showing once again that the critical determinant for toxicity is the size of the AgNPs. This size dependency of toxicity has been described for free AgNPs on macrophages [69,70] and on other mammalian cells [71]. A comparative analysis of our results with those of the literature showed that, at equal AgNP size of 10 nm, the toxicity of the hybrids on

macrophages (EC50 15.5–20  $\mu\text{g Ag/mL}$ ) was similar to that of free, citrate-coated nanoparticles (16.9  $\mu\text{g Ag/mL}$ ) on fibroblasts, [71], but lower than that of silica-supported uncoated nanoparticles (10  $\mu\text{g Ag/mL}$ ) on macrophages [72].

This means that it is quite difficult to know whether the observed toxicity arose from a pure nanoparticles effect or from an intracellular dissolution of the nanoparticles and liberation of toxic  $\text{Ag}^+$  ions. The latter hypothesis is favored in the literature [35] and it is rooted in from the fact that nanomaterials are confined in the lysosomes in animal cells, and thus cannot exert general cellular toxicity, and in the fact that intracellular AgNP dissolution was documented [73]. In line with these observations, intracellular release of  $\text{Ag}^+$  ions from AgNPs was observed in the same cell type (macrophages) here used for toxicological testing [67,68]. Moreover, studies on the same macrophage cells with silver ion showed an EC20 at 1.6  $\mu\text{g/mL}$  [67], i.e., close to the EC20 close to 4–5  $\mu\text{g/mL}$  shown here with the hybrids with small nanoparticles. Thus, overall, it is likely that the toxicity of the hybrids for animal cells arises mainly from the release of toxic silver ion.

We also explored the functional effects of the hybrids at non-toxic concentrations. We first investigated the effects on the phagocytic capacity of the cells, i.e., their ability to ingest pathogens such as bacteria. The results reported in Figure 6a showed a major effect of the hybrids on the proportion of phagocytic cells. However, this effect was mainly due to the CNCs and did not depend on the AgNP concentration. The absence of the effect of AgNP on the phagocytic capacity at non-toxic concentrations has been previously described [67]. In addition to the proportion of phagocytic cells, we also investigated if the cells that were positive for phagocytosis under different conditions were able to internalize the same number of fluorescent beads. A slight, but significant effect was observed (Figure 6b), even if it remained constant regardless of the material used, and was thus provoked by the presence of CNCs. This inhibitory effect of high concentrations of CNCs on phagocytosis is consistent with previous studies in the literature [74].

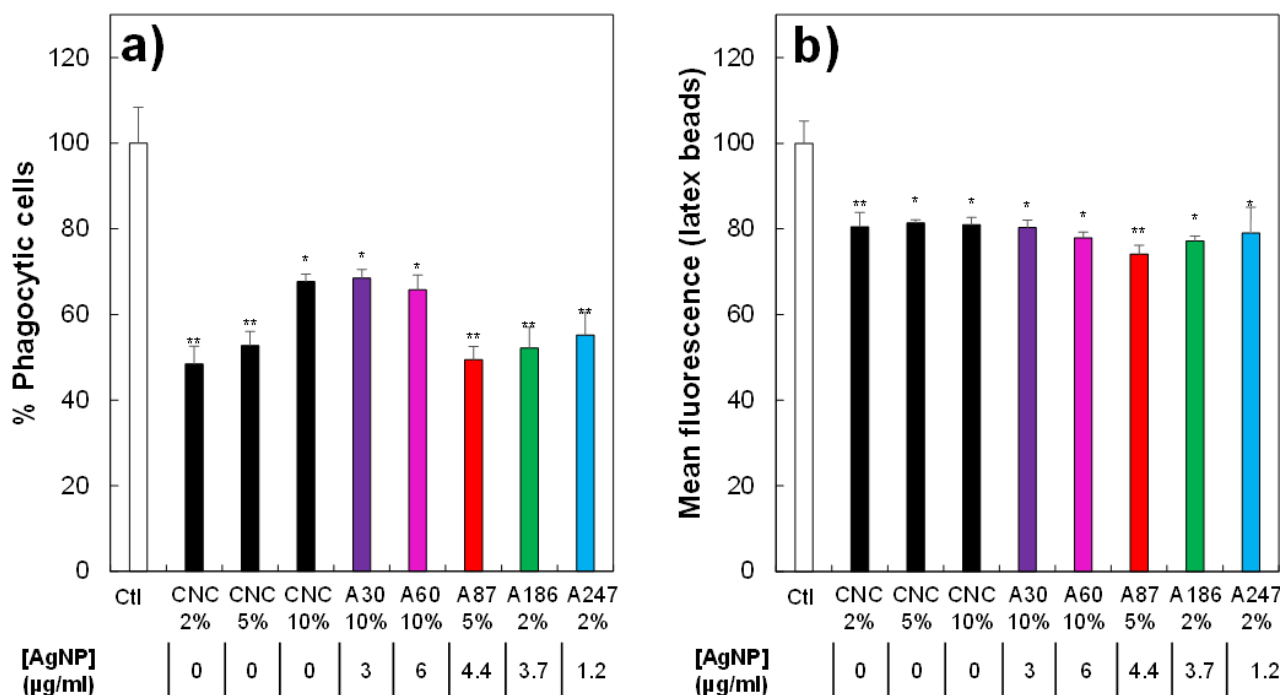


**Figure 6.** Effects of biocides on the phagocytic capacity of J774A1. (a) Proportion of phagocytic cells (in the viable cell population only) for control cells or cells treated for 24 h with different biocide concentrations; (b) mean fluorescence of phagocytic cells (in the viable cell population only) for control cells or cells treated for 24 h with different concentrations of biocides. Selected biocide concentration = before reaching lethal dose 20. Symbols indicate the statistical significance (Student's *t*-test): \*  $p < 0.05$ ; \*\*  $p < 0.01$ .

Finally, we tested the capability of the CNC/AgNP hybrids to induce an inflammatory reaction in macrophages by measuring the secretion of the pro-inflammatory cytokines TNF- $\alpha$  and interleukin IL-6 (Figure 7a,b, respectively). Concerning TNF- $\alpha$ , a synergistic effect of CNCs and AgNP was detected, making it difficult to clearly define their respective roles in the inflammatory process. On the other hand, very low production of pro-inflammatory cytokines was observed for IL-6 A, probably induced by high concentrations of CNCs alone and not by the presence of the grafted AgNPs, as previously observed for long silver nanowires [75] or for pure CNC [74,76]. Overall, the presence of the hybrids did not show an increased toxicity for macrophages compared with free AgNPs, and their functional effects on macrophages were mostly triggered by the CNC moiety, independently of the AgNP content.

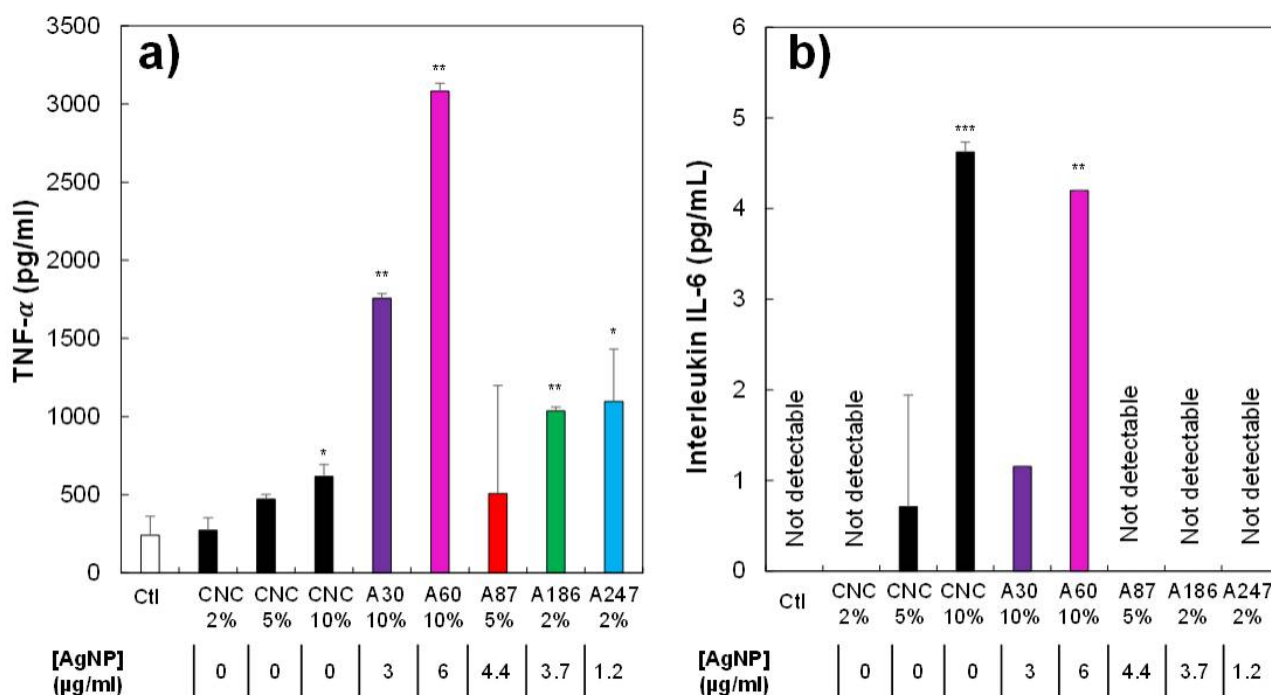


**Figure 7.** Effects of biocides on the inflammatory response of J774A1. (a) TNF- $\alpha$  production of cells only (white bar) or cells treated for 24 h with different concentrations of biocides; (b) IL-6 production of cells only or cells treated for 24 h with different concentrations of biocides. Selected biocide concentration = before reaching lethal dose 20. Symbols indicate the statistical significance (Student's *t*-test): \*  $p < 0.05$ ; \*\*  $p < 0.01$ ; \*\*\*  $p < 0.001$ .

#### 4. Conclusions

In this study, we focused on the link between the physico-chemical, morphological, and structural characteristics of AgNPs in CNC/AgNP hybrid suspensions and their biocidal and toxicological properties.

Firstly, the proposed simple process including the chemical reduction of Ag<sup>+</sup> ions using NaBH<sub>4</sub> allows the nucleation and growth of well-dispersed AgNPs on the CNC surface. No CNC surface pre-treatment was required to obtain AgNPs highly dispersible in aqueous medium. The AgNP content was varied between 0.4 and 24.7 wt%, with a narrow size-distribution of about 10 nm, whereas the amount of metallic silver (Ag<sub>0</sub>) estimated by XANES decreased with the reduction of the initial NaBH<sub>4</sub>/AgNO<sub>3</sub> molar ratio from 68 to 1.5.

An H<sub>2</sub>O<sub>2</sub> redox post-treatment made it possible to adjust the morphological properties of the primary AgNPs. When the H<sub>2</sub>O<sub>2</sub>/AgNP mass ratio ( $\alpha$ ) was higher than 0.20, an efficient AgNP size–shape transition from ~10 nm AgNPs particles to ~300 nm AgNP prisms occurred, which was associated with an increase in Ag<sub>0</sub> content up to 97%, while preserving the initial fcc structure.

The physico-chemical, morphological, and structural properties of the AgNPs in CNC/AgNP hybrids were associated with their antibacterial effect on *B. subtilis*. At 48 h, biocidal activity increased with the increase of the silver content in CNC/AgNP hybrids, but the oxidation state of AgNPs in hybrids ( $\text{Ag}^+/\text{Ag}_0$  ratio) did not trigger the short-term biocidal effect. In particular, AgNPs synthesized at a very low  $\text{NaBH}_4/\text{AgNO}_3$  molar ratio also provided an efficient antimicrobial activity. Such a result opens the way to an eco-friendlier AgNP synthesis with a noticeable decreased amount of chemical reducer. The evaluation of the short-term biocidal activity allowed us to determine an MIC of 0.016 mg AgNP/mL of hybrid. Such an MIC corresponded to an effective AgNP amount deposited on the diffusion disk of 0.048  $\mu\text{g}$  of AgNP. To the best of our knowledge, this is the lowest AgNP content that makes it possible to obtain a well-detectable biocidal effect. These results proved that the control of AgNP properties and distribution on a substrate allow strongly reducing the silver content without being detrimental to the biocidal activity, and recovering a bio-degradable cellulosic substrate after use of the material, thus reducing the environmental impact.

No biocidal activity was detected at 48 h when the  $\text{H}_2\text{O}_2$  post-treatment induced a transition to the larger 300 nm AgNP prisms. This result agrees with the lower  $\text{Ag}^+$  released with the increase in particle size (i.e., reduction of the NP specific surface area).

We also proposed a specific method to experimentally detect a long-term biocidal activity of up to 168 h. As for the tests at 48 h, smaller spherical AgNPs provided the most efficient long-term biocidal activity, while larger AgNP prisms (150–300 nm) inhibited the antibacterial effect. However, when the  $\text{H}_2\text{O}_2$  redox post-treatment did not induce large particles, the oxidation-reduction steps seemed to favor the  $\text{Ag}^+$  release. To the best of our knowledge, this is the first experimental study where the long-term antibacterial activity is measured. Furthermore, the precise comparative study of well-dispersed spherical AgNPs and AgNP prisms led to conclusive results on the inefficiency of AgNP prisms compared with smaller Ag nanospheres.

Finally, the toxicological results showed no specific impact of AgNP when it was grafted on the CNC substrate. As CNCs were previously shown to solely promote pulmonary toxicity and only at high concentrations, it is advisable to take precautions to limit their aerosolization. In this respect, the fact that the hybrid synthesis takes place via a wet route and that the end product is a suspension that can be directly used in applications is a positive aspect.

To conclude, it is by nature impossible to obtain a biocidal product that is both highly efficient and totally harmless for humans and the environment. The present results offer a very complete safe-by-design reflection on the preparation of a biocidal product. The present study allows a highly controlled amount of AgNPs to be used with high efficiency in anticipation of the release of a cellulose-safe product into the environment after use. This precisely designed bio-based biocidal material opens the way for many applications such as medical instruments or devices, wastewater treatment, food packaging and processing, or paints with biocidal properties, where the AgNP content and properties can be optimized as a function of the desired antibacterial effect.

**Supplementary Materials:** The following are available online at <https://www.mdpi.com/article/10.3390/nano11071862/s1>: Figure S1: (a) Size distribution histograms of AgNPs in CNC/AgNP hybrids at various AgNP content (b) XRD diffractograms. (c) Example of a XANES spectrum and its corresponding linear combination fit (LCF) using Ag foil and  $\text{AgNO}_3$  aqueous solution as components; (d) XANES data of CNC/AgNP hybrids at various AgNP content. Figure S2: (a) EXAFS spectra Fourier transform (solid gray lines) and fit (dotted lines); (b,c) magnitude and imaginary part (solid gray lines) and fit (dotted lines) of the Fourier transform of hybrids at various AgNP contents. Figure S3:  $\text{Ag}^+$  release kinetics over 168 h from AgNPs of hybrid NPs in an aqueous medium. Figure S4: Images of biocide-impregnated paper disks used in diffusion tests for CNC/AgNP hybrids at various AgNP contents. Figure S5:  $\text{Ag}^+$  release at 48 h in aqueous medium for CNC/AgNP hybrids at various AgNP content estimated by conductimetry. Figure S6: Inhibition halos of hybrid samples used in biocide test to discriminate the antibacterial activity of  $\text{Ag}^0$  and  $\text{Ag}^+$  fractions in AgNPs.



Figure S7: Ag<sup>+</sup> release kinetics monitored by conductimetry in aqueous medium over the time for CNC/AgNP hybrids at various AgNP content with and without H<sub>2</sub>O<sub>2</sub> redox post-treatment (i.e., 160 µL H<sub>2</sub>O<sub>2</sub>). Figure S8: Comparison between long-term diffusion tests for CNC/AgNP hybrids at various AgNP contents with and without H<sub>2</sub>O<sub>2</sub> redox post-treatment. Cases of complete and incomplete bacterial inhibition (i.e., lysis) are indicated. Table S1: R-factor and Chi-square values for linear combination fitting procedure applied to the XANES region of CNC/AgNP hybrid suspensions at different AgNP contents. Table S2: EXAFS fit results for CNC/AgNP hybrid suspensions with increasing AgNP content. Table S3: Comparison of MIC in various hybrid systems reported in the literature.

**Author Contributions:** Conceptualization, methodology, data curation, and original draft writing: I.C. and D.M.; Microscopy acquisition analysis: D.M.; XANES-EXAFS measurements, data analysis, and discussion: C.R., G.L., D.M. and I.C.; Biocidal activity tests: T.R., C.L. and S.L.; Toxicological tests: T.R., J.D. and B.D.; Supervision, project administration, funding acquisition: I.C.; All authors have read and agreed to the published version of the manuscript.

**Funding:** This work is a contribution to the Labex SERENADE (n° ANR-11-LABX-0064) funded by the “Investissement d’Avenir” French government program of the French National Research Agency (ANR) through the A\*MIDEX project (n° ANR-11-IDEX-0001-02).

**Data Availability Statement:** Additional results are in supporting information, no other publicly archived datasets analyzed or generated during the study.

**Acknowledgments:** We acknowledge SOLEIL for providing access to its synchrotron radiation facilities on the SAMBA beamline. We gratefully acknowledge S. Durand (BIA-Nantes) for support in FTIR measurements, F. X. Lefevre and N. Guichard (Université de Nantes) for support in AAS experiments, B. Pontoire (BIA-Nantes) for performing XRD acquisitions, B. Novales for helping in acquisition of STEM images, and S. Haouache (BIA-Nantes) for helping during SAMBA beamtime. This work is a contribution to the Labex SERENADE (n° ANR-11-LABX-0064) funded by the French government program, “Investissement d’Avenir”, of the French National Research Agency (ANR) through the A\*MIDEX project (n° ANR-11-IDEX-0001-02).

**Conflicts of Interest:** The authors declare no conflict of interest.

## References

1. Xiu, Z.M.; Zhang, Q.B.; Puppala, H.L.; Colvin, V.L.; Alvarez, P.J.J. Negligible particle-specific antibacterial activity of silver nanoparticles. *Nano Lett.* **2012**, *12*, 4271–4275. [[CrossRef](#)] [[PubMed](#)]
2. Morones, J.R.; Elechiguerra, J.L.; Camacho, A.; Holt, K.; Kouri, J.B.; Ramirez, J.T.; Yacaman, M.J. The bactericidal effect of silver nanoparticles. *Nanotechnology* **2005**, *16*, 2346–2353. [[CrossRef](#)]
3. Sharma, V.K.; Yngard, R.A.; Lin, Y. Silver nanoparticles: Green synthesis and their antimicrobial activities. *Adv. Colloid Interface Sci.* **2009**, *145*, 83–96. [[CrossRef](#)] [[PubMed](#)]
4. Harish, B.S.; Uppuluri, K.B.; Anbazhagan, V. Synthesis of fibrinolytic active silver nanoparticle using wheat bran xylan as a reducing and stabilizing agent. *Carbohydr. Polym.* **2015**, *132*, 104–110. [[CrossRef](#)]
5. Edge, M.; Allen, N.S.; Turner, D.; Robinson, J.; Seal, K. The enhanced performance of biocidal additives in paints and coatings. *Prog. Org. Coatings* **2001**, *43*, 10–17. [[CrossRef](#)]
6. Pulit-Prociak, J.; Chwastowski, J.; Siudek, M.; Banach, M. Incorporation of Metallic Nanoparticles into Cosmetic Preparations and Assessment of Their Physicochemical and Utility Properties. *J. Surfactants Deterg.* **2018**, *21*, 575–591. [[CrossRef](#)]
7. Wu, D.M.; Fan, W.; Kishen, A.; Gutmann, F.B. Evaluation of the Antibacterial Efficacy of Silver Nanoparticles against *Enterococcus faecalis* Biofilm. *J. Endod.* **2014**, *40*, 285–290. [[CrossRef](#)]
8. Yahyaei, B.; Azizian, S.; Mohammadzadeh, A.; Pajohi-Alamoti, M. Preparation of clay/alumina and clay/alumina/Ag nanoparticle composites for chemical and bacterial treatment of waste water. *Chem. Eng. J.* **2014**, *247*, 16–24. [[CrossRef](#)]
9. Ruparelia, J.P.; Chatterjee, A.K.; Duttagupta, S.P.; Mukherji, S. Strain specificity in antimicrobial activity of silver and copper nanoparticles. *Acta Biomater.* **2008**, *4*, 707–716. [[CrossRef](#)]
10. Rai, M.; Yadav, A.; Gade, A. Silver nanoparticles as a new generation of antimicrobials. *Biotechnol. Adv.* **2009**, *27*, 76–83. [[CrossRef](#)] [[PubMed](#)]
11. Klaseen, H. A historical review of the use of silver in the treatment of burns. II. Renewed interest for silver. *Burns* **2000**, *26*, 117–130. [[CrossRef](#)]
12. Liao, S.Y.; Read, D.C.; Pugh, W.J.; Furr, J.R.; Russell, A.D. Interaction of silver nitrate with readily identifiable groups: Relationship to the antibacterial action of silver ions. *Lett. Appl. Microbiol.* **1997**, *25*, 279–283. [[CrossRef](#)] [[PubMed](#)]
13. Feng, Q.L.; Wu, J.; Chen, G.Q.; Cui, F.Z.; Kim, T.N.; Kim, J.O. A mechanistic study of the antibacterial effect of silver ions on *Escherichia coli* and *Staphylococcus aureus*. *J. Biomed. Mater. Res.* **2000**, *52*, 662–668. [[CrossRef](#)]

14. Ho, C.H.; Odermatt, E.K.; Berndt, I.; Joerg, C. Long-term active antimicrobial coatings for surgical sutures based on silver nanoparticles and hyperbranched polylysine. *J. Biomater. Sci. Polym. Ed.* **2013**, *24*, 1589–1600. [[CrossRef](#)]
15. Korani, M.; Ghazizadeh, E.; Korani, S.; Hami, Z.; Mohammadi-Bardbori, A. Effects of silver nanoparticles on human health. *Eur. J. Nanomed.* **2015**, *7*, 51–62. [[CrossRef](#)]
16. Ferdous, Z.; Nemmar, A. Health Impact of Silver Nanoparticles: A Review of the Biodistribution and Toxicity Following Various Routes of Exposure. *Int. J. Mol. Sci.* **2020**, *21*, 2375. [[CrossRef](#)]
17. León-Silva, S.; Fernández-Luqueño, F.; López-Valdez, F. Silver Nanoparticles (AgNP) in the Environment: A Review of Potential Risks on Human and Environmental Health. *Water Air Soil Pollut.* **2016**, *227*, 1–20. [[CrossRef](#)]
18. Panyala, N.R.; Peña-Méndez, E.M.; Havel, J. Silver or silver nanoparticles: A hazardous threat to the environment and human health? *J. Appl. Biomed.* **2008**, *6*, 117–129. [[CrossRef](#)]
19. Li, S.; Zhang, Y.; Xu, X.; Zhang, L. Triple Helical Polysaccharide-Induced Good Dispersion of Silver Nanoparticles in Water. *Biomacromolecules* **2011**, *26*, 2864–2871. [[CrossRef](#)]
20. Vimala, K.; Mohan, Y.M.; Sivudu, K.S.; Varaprasad, K.; Ravindra, S.; Reddy, N.N.; Padma, Y.; Sreedhar, B.; Mohanaraju, K. Fabrication of porous chitosan films impregnated with silver nanoparticles: A facile approach for superior antibacterial application. *Colloids Surf. B Biointerfaces* **2010**, *76*, 248–258. [[CrossRef](#)]
21. Vimala, K.; Sivudu, K.S.; Mohan, Y.M.; Sreedhar, B.; Raju, K.M. Controlled silver nanoparticles synthesis in semi-hydrogel networks of poly (acrylamide) and carbohydrates: A rational methodology for antibacterial application. *Carbohydr. Polym.* **2009**, *75*, 463–471. [[CrossRef](#)]
22. Brinchi, L.; Cotana, F.; Fortunati, E.; Kenny, J.M. Production of nanocrystalline cellulose from lignocellulosic biomass: Technology and applications. *Carbohydr. Polym.* **2013**, *94*, 154–169. [[CrossRef](#)]
23. Reid, M.S.; Villalobos, M.; Cranston, E.D. Benchmarking Cellulose Nanocrystals: From the Laboratory to Industrial Production. *Langmuir* **2017**, *33*, 1583–1598. [[CrossRef](#)]
24. Tsuji, M.; Gomi, S.; Maeda, Y.; Matsunaga, M.; Hikino, S.; Uto, K.; Tsuji, T.; Kawazumi, H. Rapid transformation from spherical nanoparticles, nanorods, cubes, or bipyramids to triangular prisms of silver with PVP, citrate, and H<sub>2</sub>O<sub>2</sub>. *Langmuir* **2012**, *28*, 8845–8861. [[CrossRef](#)]
25. Guzman, M.; Dille, J.; Godet, S. Synthesis and antibacterial activity of silver nanoparticles against gram-positive and gram-negative bacteria. *Nanomed. Nanotechnol. Biol. Med.* **2012**, *8*, 37–45. [[CrossRef](#)]
26. Pastoriza-santos, I.; Liz-marza, L.M. Synthesis of Silver Nanoprisms in DMF. *Nano Lett.* **2002**, *2*, 903–905. [[CrossRef](#)]
27. Yang, G.; Xie, J.; Hong, F.; Cao, Z.; Yang, X. Antimicrobial activity of silver nanoparticle impregnated bacterial cellulose membrane: Effect of fermentation carbon sources of bacterial cellulose. *Carbohydr. Polym.* **2012**, *87*, 839–845. [[CrossRef](#)]
28. Jiang, F.; Hsieh, Y. Lo Synthesis of cellulose nanofibril bound silver nanoprism for surface enhanced raman scattering. *Biomacromolecules* **2014**, *15*, 3608–3616. [[CrossRef](#)] [[PubMed](#)]
29. Lokanathan, A.R.; Uddin, K.M.A.; Rojas, O.J.; Laine, J. Cellulose nanocrystal-mediated synthesis of silver nanoparticles: Role of sulfate groups in nucleation phenomena. *Biomacromolecules* **2014**, *15*, 373–379. [[CrossRef](#)] [[PubMed](#)]
30. Ling, G.; He, J.; Huang, L. Size control of silver nanoparticles deposited on silica dielectric spheres by electroless plating technique. *J. Mater. Sci.* **2004**, *39*, 2955–2957. [[CrossRef](#)]
31. Shi, Z.; Tang, J.; Chen, L.; Yan, C.; Tanvir, S.; Anderson, W.A.; Berry, R.M.; Tam, K.C. Enhanced Colloidal Stability and Antibacterial Performance of Silver Nanoparticles/Cellulose Nanocrystal Hybrids. *J. Mater. Chem. B* **2015**, *3*, 603–611. [[CrossRef](#)]
32. Nickel, U.; Castell, A.Z.; Pöppl, K.; Schneider, S. Silver colloid produced by reduction with hydrazine as support for highly sensitive surface-enhanced Raman spectroscopy. *Langmuir* **2000**, *16*, 9087–9091. [[CrossRef](#)]
33. Kaushik, M.; Moores, A. Review: Nanocelluloses as versatile supports for metal nanoparticles and their applications in catalysis. *Green Chem.* **2016**, *18*, 622–637. [[CrossRef](#)]
34. Musino, D.; Rivard, C.; Novales, B.; Landrot, G.; Rabilloud, T.; Capron, I. Hydroxyl Groups on Cellulose Nanocrystal Surfaces form Nucleation Points for Silver Nanoparticles of Varying Shapes and Sizes (Accepted). *J. Colloid Interface Sci.* **2021**, *584*, 360–371. [[CrossRef](#)] [[PubMed](#)]
35. Le Ouay, B.; Stellacci, F. Antibacterial activity of silver nanoparticles: A surface science insight. *Nano Today* **2015**, *10*, 339–354. [[CrossRef](#)]
36. Espinosa-Cristóbal, L.F.; Martínez-Castañón, G.A.; Martínez-Martínez, R.E.; Loyola-Rodríguez, J.P.; Patiño-Marín, N.; Reyes-Macías, J.F.; Ruiz, F. Antibacterial effect of silver nanoparticles against *Streptococcus mutans*. *Mater. Lett.* **2009**, *63*, 2603–2606. [[CrossRef](#)]
37. Martínez-Castañón, G.A.; Nino-Martinez, N.; Martinez-Gutierrez, F.; Martinez-Mendoza, J.R.; Ruiz, F. Synthesis and antibacterial activity of silver nanoparticles with different sizes. *J. Nanopart. Res.* **2008**, *10*, 1343–1348. [[CrossRef](#)]
38. Drogat, N.; Granet, R.; Sol, V.; Memmi, A.; Saad, N.; Klein Koerkamp, C.; Bressollier, P.; Krausz, P. Antimicrobial silver nanoparticles generated on cellulose nanocrystals. *J. Nanopart. Res.* **2011**, *13*, 1557–1562. [[CrossRef](#)]
39. Errokh, A.; Magnin, A.; Putaux, J.L.; Boufi, S. Hybrid nanocellulose decorated with silver nanoparticles as reinforcing filler with antibacterial properties. *Mater. Sci. Eng. C* **2019**, *105*, 110044. [[CrossRef](#)]
40. Kim, T.H.; Kim, M.; Park, H.S.; Shin, U.S.; Gong, M.S.; Kim, H.W. Size-dependent cellular toxicity of silver nanoparticles. *J. Biomed. Mater. Res. Part A* **2012**, *100*, 1033–1043. [[CrossRef](#)]

41. Dong, S.; Hirani, A.A.; Colacino, K.R.; Lee, Y.W.; Roman, M. Cytotoxicity and Cellular Uptake of Cellulose Nanocrystals. *Nano Life* **2012**, *2*, 1241006. [[CrossRef](#)]
42. Catalan, J.; Ilves, M.; Jarventausta, H.; Hannukainen, K.-S.; Kontturi, E.; Vanhala, E.; Alenius, H.; Savolainen, K.M.; Norppa, H. Genotoxic and Immunotoxic Effects of Cellulose Nanocrystals In Vitro. *Environ. Mol. Mutagen.* **2015**, *56*, 171–182. [[CrossRef](#)] [[PubMed](#)]
43. Roman, M. Toxicity of cellulose nanocrystals: A review. *Ind. Biotechnol.* **2015**, *11*, 25–33. [[CrossRef](#)]
44. Park, E.J.; Khaliullin, T.O.; Shurin, M.R.; Kisin, E.R.; Yanamala, N.; Fadeel, B.; Chang, J.; Shvedova, A.A. Fibrous nanocellulose, crystalline nanocellulose, carbon nanotubes, and crocidolite asbestos elicit disparate immune responses upon pharyngeal aspiration in mice. *J. Immunotoxicol.* **2018**, *15*, 12–23. [[CrossRef](#)]
45. Pal, S.; Tak, Y.K.; Song, J.M. Does the Antibacterial Activity of Silver Nanoparticles Depend on the Shape of the Nanoparticle? A Study of the Gram-Negative Bacterium *Escherichia coli*. *Appl. Environ. Microbiol.* **2007**, *73*, 1712–1720. [[CrossRef](#)] [[PubMed](#)]
46. Parnklang, T.; Lamlua, B.; Gatemala, H.; Thammacharoen, C.; Kuimalee, S.; Lohwongwatana, B.; Ekgasit, S. Shape transformation of silver nanospheres to silver nanoplates induced by redox reaction of hydrogen peroxide. *Mater. Chem. Phys.* **2015**, *153*, 127–134. [[CrossRef](#)]
47. Métraux, G.S.; Mirkin, C.A. Rapid thermal synthesis of silver nanoprisms with chemically tailorable thickness. *Adv. Mater.* **2005**, *17*, 412–415. [[CrossRef](#)]
48. Millstone, J.E.; Hurst, S.J.; Métraux, G.S.; Cutler, J.I.; Mirkin, C.A. Colloidal gold and silver triangular nanoprisms. *Small* **2009**, *5*, 646–664. [[CrossRef](#)] [[PubMed](#)]
49. Van Dong, P.; Ha, C.H.; Binh, L.T.; Kasbohm, J. Chemical synthesis and antibacterial activity of novel-shaped silver nanoparticles. *Int. Nano Lett.* **2012**, *2*, 1–9. [[CrossRef](#)]
50. Raza, M.A.; Kanwal, Z.; Rauf, A.; Sabri, A.N.; Riaz, S.; Naseem, S. Size- and shape-dependent antibacterial studies of silver nanoparticles synthesized by wet chemical routes. *Nanomaterials* **2016**, *6*, 74. [[CrossRef](#)] [[PubMed](#)]
51. Badawy, A.M.E.L.; Silva, R.G.; Morris, B.; Scheckel, K.G.; Suidan, M.T. Surface Charge-Dependent Toxicity of Silver Nanoparticles. *Environ. Sci. Technol.* **2011**, *45*, 283–287. [[CrossRef](#)]
52. Yang, X.; Gondikas, A.P.; Marinakos, S.M.; Auffan, M.; Liu, J.; Hsu-kim, H.; Meyer, J.N. Mechanism of Silver Nanoparticle Toxicity Is Dependent on Dissolved Silver and Surface Coating in *Caenorhabditis elegans*. *Environ. Sci. Technol.* **2012**, *46*, 1119–1127. [[CrossRef](#)] [[PubMed](#)]
53. Ma, R.; Levard, C.; Marinakos, S.M.; Cheng, Y.; Liu, J.; Michel, F.M.; Brown, G.E.; Lowry, G.V. Size-controlled dissolution of organic-coated silver nanoparticles. *Environ. Sci. Technol.* **2012**, *46*, 752–759. [[CrossRef](#)] [[PubMed](#)]
54. Marambio-Jones, C.; Hoek, E.M.V. A review of the antibacterial effects of silver nanomaterials and potential implications for human health and the environment. *J. Nanopart. Res.* **2010**, *12*, 1531–1551. [[CrossRef](#)]
55. Kumar, A.; Vemula, P.K.; Ajayan, P.M.; John, G. Silver-nanoparticle-embedded antimicrobial paints based on vegetable oil. *Nat. Mater.* **2008**, *7*, 236–241. [[CrossRef](#)] [[PubMed](#)]
56. Musino, D.; Rivard, C.; Landrot, G.; Novales, B.; Capron, I. Tunable Ag Nanoparticle Properties in Cellulose Nanocrystals/Ag Nanoparticle Hybrid Suspensions by H<sub>2</sub>O<sub>2</sub> Redox Post-Treatment: The Role Of The H<sub>2</sub>O<sub>2</sub>/Ag Ratio. *Nanomaterials* **2020**, *10*, 1559. [[CrossRef](#)] [[PubMed](#)]
57. Ravel, B.; Newville, M. Athena, artemis, hephaestus: Data analysis for X-ray absorption spectroscopy using IFEFFIT. *J. Synchrotron Radiat.* **2005**, *12*, 537–541. [[CrossRef](#)]
58. Suh, I.K.; Ohta, H.; Waseda, Y. High-temperature thermal expansion of six metallic elements measured by dilatation method and X-ray diffraction. *J. Mater. Sci.* **1988**, *23*, 757–760. [[CrossRef](#)]
59. Singhsa, P.; Narain, R.; Manuspriya, H. Bacterial Cellulose Nanocrystals (BCNC) Preparation and Characterization from Three Bacterial Cellulose Sources and Development of Functionalized BCNCs as Nucleic Acid Delivery Systems. *ACS Appl. Nano Mater.* **2018**, *1*, 209–221. [[CrossRef](#)]
60. Kelly, S.D.; Hesterberg, D.; Ravel, B. Analysis of Soils and Minerals Using X-ray Absorption Spectroscopy. *Mineral. Methods* **2015**, *5*, 387–463. [[CrossRef](#)]
61. Zhang, W.; Yao, Y.; Sullivan, N.; Chen, Y. Modeling the primary size effects of citrate-coated silver nanoparticles on their ion release kinetics. *Environ. Sci. Technol.* **2011**, *45*, 4422–4428. [[CrossRef](#)] [[PubMed](#)]
62. Usman, M.S.; El Zowalaty, M.E.; Shameli, K.; Zainuddin, N.; Salama, M.; Ibrahim, N.A. Synthesis, characterization, and antimicrobial properties of copper nanoparticles. *Int. J. Nanomed.* **2013**, *8*, 4467–4479. [[CrossRef](#)]
63. Gopinath, V.; MubarakAli, D.; Priyadarshini, S.; Priyadharshini, N.M.; Thajuddin, N.; Velusamy, P. Biosynthesis of silver nanoparticles from *Tribulus terrestris* and its antimicrobial activity: A novel biological approach. *Colloids Surf. B Biointerfaces* **2012**, *96*, 69–74. [[CrossRef](#)]
64. Shaheen, T.I.; Fouda, A. International Journal of Biological Macromolecules Green approach for one-pot synthesis of silver nanorod using cellulose nanocrystal and their cytotoxicity and antibacterial assessment. *Int. J. Biol. Macromol.* **2018**, *106*, 784–792. [[CrossRef](#)] [[PubMed](#)]
65. Merrill, C. Development and Mechanisms of Silver Stains for Electrophoresis. *ACTA Histochem. Cytochem.* **1986**, *19*, 655–667. [[CrossRef](#)]
66. Gianazza, E.; Astrua-Testori, S.; Righetti, P.G. Some more formulations for immobilized pH gradients. *Electrophoresis* **1985**, *6*, 113–117. [[CrossRef](#)]

67. Dalzon, B.; Torres, A.; Diemer, H.; Ravanel, S.; Collin-Faure, V.; Pernet-Gallay, K.; Jouneau, P.H.; Bourguignon, J.; Cianfèrani, S.; Carrière, M.; et al. How reversible are the effects of silver nanoparticles on macrophages? A proteomic-instructed view. *Environ. Sci. Nano* **2019**, *6*, 3133–3157. [[CrossRef](#)]
68. Dalzon, B.; Aude-Garcia, C.; Diemer, H.; Bons, J.; Marie-Desvergne, C.; Pérard, J.; Dubosson, M.; Collin-Faure, V.; Carapito, C.; Cianfèrani, S.; et al. The longer the worse: A combined proteomic and targeted study of the long-term: Versus short-term effects of silver nanoparticles on macrophages. *Environ. Sci. Nano* **2020**, *7*, 2032–2046. [[CrossRef](#)]
69. Park, M.V.D.Z.; Neigh, A.M.; Vermeulen, J.P.; de la Fonteyne, L.J.J.; Verharen, H.W.; Briedé, J.J.; van Loveren, H.; de Jong, W.H. The effect of particle size on the cytotoxicity, inflammation, developmental toxicity and genotoxicity of silver nanoparticles. *Biomaterials* **2011**, *32*, 9810–9817. [[CrossRef](#)] [[PubMed](#)]
70. Park, J.; Lim, D.H.; Lim, H.J.; Kwon, T.; Choi, J.S.; Jeong, S.; Choi, I.H.; Cheon, J. Size dependent macrophage responses and toxicological effects of Ag nanoparticles. *Chem. Commun.* **2011**, *47*, 4382–4384. [[CrossRef](#)] [[PubMed](#)]
71. Ivask, A.; Kurvet, I.; Kasemets, K.; Blinova, I.; Aruoja, V.; Suppi, S.; Vija, H.; Kakinen, A.; Titma, T.; Heinlaan, M.; et al. Size-dependent toxicity of silver nanoparticles to bacteria, yeast, algae, crustaceans and mammalian cells in vitro. *PLoS ONE* **2014**, *9*, e102108. [[CrossRef](#)]
72. Pratsinis, A.; Hervella, P.; Leroux, J.C.; Pratsinis, S.E.; Sotiriou, G.A. Toxicity of silver nanoparticles in macrophages. *Small* **2013**, *9*, 2576–2584. [[CrossRef](#)] [[PubMed](#)]
73. Gliga, A.; Skoglund, S.; Wallinder, I.; Fadeel, B.; Karlsson, H. Size-dependent cytotoxicity of silver nanoparticles in human lung cells: The role of cellular uptake, agglomeration and Ag release. *Part. Fibre Toxicol.* **2014**, *17*, 11. [[CrossRef](#)]
74. Samulin Erdem, J.; Alswady-Hoff, M.; Ervik, T.K.; Skare, Ø.; Ellingsen, D.G.; Zienolddiny, S. Cellulose nanocrystals modulate alveolar macrophage phenotype and phagocytic function. *Biomaterials* **2019**, *203*, 31–42. [[CrossRef](#)] [[PubMed](#)]
75. Toybou, D.; Celle, C.; Aude-Garcia, C.; Rabilloud, T. A toxicology-informed, safer by design approach for the fabrication of transparent electrodes based on silver nanowires. *Environ. Sci. Nano* **2019**, *6*, 684–694. [[CrossRef](#)]
76. Shvedova, A.A.; Kisin, E.R.; Yanamala, N.; Farcas, M.T.; Menas, A.L.; Williams, A.; Fournier, P.M.; Reynolds, J.S.; Gutkin, D.W.; Star, A.; et al. Gender differences in murine pulmonary responses elicited by cellulose nanocrystals. *Part. Fibre Toxicol.* **2016**, *13*, 1–20. [[CrossRef](#)]